Adjustment of Block Copolymer Nanodomain Sizes at Lattice Defect Sites

Matthew R. Hammond, Scott W. Sides, Glenn H. Fredrickson, and Edward J. Kramer*

Departments of Materials and Chemical Engineering, University of California, Santa Barbara, California 93106

Janne Ruokolainen

Helsinki University of Technology, Helsinki, Finland

Stephen F. Hahn

Corporate R&D, The Dow Chemical Company, Midland, Michigan 48674

Received December 23, 2002; Revised Manuscript Received August 29, 2003

ABSTRACT: Lattice defects in two-dimensional hexagonal arrays primarily take the form of dislocations, point defects that lie at the mutual terminus of two incomplete rows of material. The dislocation core is composed of one 5-fold and one 7-fold coordinated domain within the otherwise hexagonally coordinated lattice. Using scanning force microscopy to view the nanodomains of a 2D hexagonal array of vertically oriented poly(cyclohexylethylene)−poly(ethylene)−poly(cyclohexylethylene) (CEC) cylindrical triblock copolymers, we show that the domains which compose dislocation cores adjust their sizes (5-fold coordinated cylinders contract and 7-fold coordinated cylinders expand) in response to the stress field associated with the defect. Similar analysis was performed on a two-dimensional self-consistent mean-field theoretical simulation of a similar triblock copolymer system, yielding good agreement with experimental results.

Introduction

Recent advances in the use of block copolymer thin films as nanolithographic templates or resists in the production of electronic, magnetic, or ceramic nanodomain devices[1−3] have driven research efforts aimed at exerting better control of the long-range ordering and orientation of the copolymer nanodomain arrays. Various schemes have been introduced to control and enhance this ordering, including the use of external electric fields,[4,5] carefully controlled surface interactions,[6,7] and chemically[8,9] or topographically[10] patterned surfaces, with some success. However, an understanding of the defect structures formed in such films is important for commercial applications.

Edge dislocations are the predominant lattice defect type observed in 2D periodic hexagonal arrays, such as those formed in spherical or vertically oriented cylindrical block copolymer films.[11] In 3D, an edge dislocation is formed by the insertion of an additional half-plane of material, with the defect core located at the line formed by the edge of that half-plane. In 2D, a dislocation is encountered at the end point of two additional half-rows of material and consists of a pair of oppositely charged disclinations. These disclinations take the form of domains with five nearest neighbors (a $-\pi/3$ disclination) and seven nearest neighbors ($+\pi/3$), rather than the normal 6-fold coordination. Dislocations often occur in pairs or clusters oriented such that the net Burgers vector is zero, and the orientational mismatch at tilt grain boundaries is accommodated by lining the boundary with dislocations. Unpaired disclinations do not occur in well-ordered 2D arrays—in fact, the unbinding of dislocations into free disclinations is integral to the 2D melting process set forth by Kosterlitz, Thouless, Halperin, Nelson, and Young (KTHNY theory).[12−17]

The strain energy of a dislocation is composed of the elastic lattice strain energy E_{el}, which for a circle of radius R around the dislocation core is proportional to $\ln(R)$, and the energy associated with the dislocation core itself, E_{core}.[18] In this paper we investigate the defect structure of a film of asymmetric block copolymer whose cylinder nanodomains are oriented normal to the film plane, forming a 2D array with hexagonal packing. We show that, in response to the defect core energy, the cylinders at lattice defect sites adjust their sizes—5-fold cylinders contract and 7-fold cylinders expand—relative to cylinders with 6-fold coordination. This effect has been predicted qualitatively by an approximate mean-field theory (MFT) simulation of asymmetric diblock copolymers.[19] Here, we also compare our results with those from a full self-consistent MFT calculation and find good agreement.

Experimental Section

Materials. Poly(cyclohexylethylene)-*b*-poly(ethylene)-*b*-poly(cyclohexylethylene) (PCHE−PE−PCHE, or simply CEC) triblock copolymer was synthesized by heterogeneous catalytic hydrogenation[20] of a polystyrene-*b*-polybutadiene-*b*-polystyrene (SBS) precursor. The SBS triblock was prepared by anionic polymerization in cyclohexane; blocks were formed by sequential monomer addition, and the final triblock had a polydispersity index of 1.02. The hydrogenated polymer has M_w = 52 770 g/mol, f_{PE} = 24%, and the 10% 1,2 monomer addition in the precursor poly(butadiene) block yields an average of 26 ethyl branches per 1000 backbone carbons in the PE block. In bulk, the polymer forms hexagonally packed cylinders with a core diameter of 11 nm and a lattice repeat spacing of 21 nm.[21] This block copolymer was chosen on the basis of the following considerations: Its cylinders are large enough that they can be easily imaged by SFM—for smaller molecular weight samples the SFM error becomes very significant. Larger molecular weight samples are more strongly segregated and order very slowly.[21] Under these circumstances one cannot ensure that the cylinder domain sizes and shapes have reached equilibrium values.

---

* To whom correspondence should be addressed.

10.1021/ma026001o CCC: $25.00 © 2003 American Chemical Society
Published on Web 10/25/2003

Film Preparation. Spin-casting 1% (by weight) solutions of the copolymer in hot decahydronaphthalene (mixture of *cis*- and *trans*-decalin, Aldrich) at 2250 rpm onto hot silicon wafers resulted in uniform, 45 nm thick films. The substrate temperature was maintained at approximately 120 °C by an IR lamp equipped with a voltage regulator. The block copolymer films were subsequently annealed in high vacuum ($<10^{-6}$ Torr) at 220 °C for 7 days. This treatment produces hexagonal arrays of cylinders with PE cores that stand perpendicular to the substrate surface.[21]

Scanning Force Microscopy and Transmission Electron Microscopy. The copolymer microstructure was imaged with scanning force microscopy (SFM), using a Digital Instruments Multimode AFM operating in Tapping Mode. Contrast in the SFM images arises from the difference in mechanical properties at room temperature between the glassy PCHE matrix and the softer PE domains. The analyses were performed on 500 nm × 500 nm scans with an image resolution of 512 × 512 pixels. Transmission electron microscopy (TEM) of film cross sections was carried out using a JEOL 2000FX TEM operating at 200 kV. A thicker CEC film was spun-cast and annealed on a NaCl crystal. The film was stained with RuO_4 vapor, floated off onto the surface of a deionized water bath, and embedded in epoxy. Cross sections were microtomed at room temperature using a Leica Ultracut UCT ultramicrotome with a diamond knife.

Image Processing and Analysis. Before analyzing the PE domain areas, the images were manipulated to reduce the influence of long- and short-wavelength background noise. This was accomplished by convoluting the image, $f(\mathbf{x})$, with a Gaussian function which in Fourier space has its maximum at the first Fourier peak of $f(\mathbf{q})$, and a full width at half-maximum of $2\pi/a$, where a is the lattice spacing. This enhances the periodicity associated with the hexagonal array without introducing any artifacts.[22] Image Pro by Media Cybernetics was used to determine the centroid positions and areas of the cylinders. A Voronoi diagram was then constructed from the set of cylinder centroids in order to easily identify the individual $+\pi/3$ (7-sided) and $-\pi/3$ (5-sided) disclinations. The occasional misidentification of coordination number for cylinders at the image edges by the Voronoi algorithm was corrected by hand. Additionally, data from cylinders whose centers lay within one lattice period of the edges of the image were discarded. Given that a gray scale threshold had to be used to determine the extent of the PE domains, variations from image to image made it difficult to reproducibly measure the absolute area of the PE domains. For this reason, images were analyzed separately, and the raw domain area data from each image were normalized by the mean area of the 6-fold sites within that image to yield $A_i/\langle A_6\rangle$. The gray scale threshold value chosen did not significantly alter these normalized data.

As an alternate measure of the cylinder sizes, the areas of the Voronoi polygons themselves were also analyzed. Similarly to the treatment of the minority phase domain areas, the raw areas thus obtained were normalized by the mean area of the hexagonal Voronoi cells within a given image.

Simulation. The method employed for the self-consistent mean-field theory (SCMFT) calculations has been previously reported;[23] however, a brief summary of the relevant details is appropriate here. The method searches for low free energy solutions of the SCMFT equations in real space within a box with periodic boundary conditions, starting from randomly generated potential fields, and without any assumption of the symmetry of the resulting nanodomain structure. The simulation presented here was carried out for an A−B−A triblock copolymer (fraction of A−B−A being 0.365, 0.27, and 0.365, respectively) on a square grid of 400 × 400 lattice points, with a lattice spacing of $0.12R_g$, where R_g is the radius of gyration of the polymer in the absence of any potential. The energy scale for the simulation is set by the product of the interaction parameter and the chain length, $\chi_{AB}N$. For this study, a value of 28 was chosen for the final value of $\chi_{AB}N$ (corresponding to $N = 200$ repeat units and $\chi_{AB} = 0.14$, for example). To control certain numerical instabilities, the initial $\chi_{AB}N$ value was chosen to be smaller than the final value, i.e., 20. As the simulation revealed increasingly microphase-separated configurations for the A−B monomer densities, the value of $\chi_{AB}N$ was slowly increased to its final value.

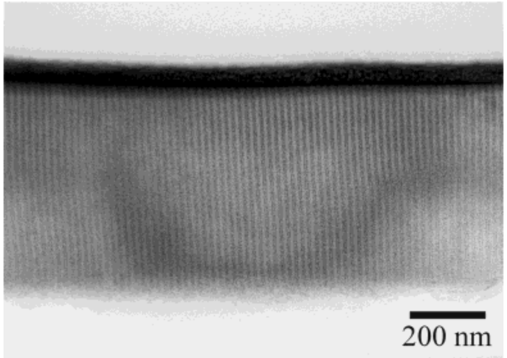

Figure 1. Cross-sectional transmission electron micrograph showing the vertical orientation of cylinders in an annealed CEC thick film. The amorphous regions of the PE cylinder cores appear dark in the image due to the RuO_4 stain. Note that the approximately 50 nm thick dark layer at the top of the film is due to contamination from the RuO_4 stain, as the staining was performed before embedding the film and subsequent cross-sectioning.

Results and Discussion

The orientation of the cylindrical nanodomains of the CEC triblock normal to the substrate surface has been previously reported[21,24] and is confirmed by cross-sectional TEM, as observed in Figure 1. The cylinders persist from the air interface (above which is a dark layer due to some deposition of the RuO_4 stain) through to the substrate interface. Though it has yet to be understood to a satisfactory level, this deviation from the more typical tendency of cylindrical nanodomains to orient with their axes parallel to the substrate can be partially explained by the very nearly equal surface energies[7] of PE (10% ethyl branching) and PCHE. The relevance of this hypothesis is corroborated by the observation that when the ethyl branching of the PE block is increased from 10% to 40%, while keeping the overall molecular weight and block fraction constant, a parallel orientation of the cylinders is observed. In that case, the extra surface-active methyl groups lower the surface energy of the PE domains, causing a PE brush layer to form at the surface.

A typical SFM image of the cylinder array is shown in Figure 2A. The softer PE domains, which appear dark, are easily distinguishable from the PCHE matrix in Tapping Mode phase images, whereas height images showed poorer contrast under the relatively light tapping conditions employed here. Figure 2A contains three isolated dislocations and a grain boundary in the upper-left portion of the image. Under the annealing conditions used in this work, paired or otherwise clustered dislocations were rarely observed, other than at grain boundaries, and unbound disclinations were never observed.

Figure 2B depicts an enlarged view of an individual dislocation in Figure 2A. Lines are drawn indicating the two extra rows of cylinders that terminate at the 5-fold site, and the 7-fold site is indicated with a yellow dot. The 5- and 7-fold sites are noticeably smaller and larger, respectively, than the 6-fold-coordinated sites that surround them.

Gaussian image enhancement (Figure 2C) facilitated the binarization of the image while preserving the defect structures in the parent image. The Voronoi construc-

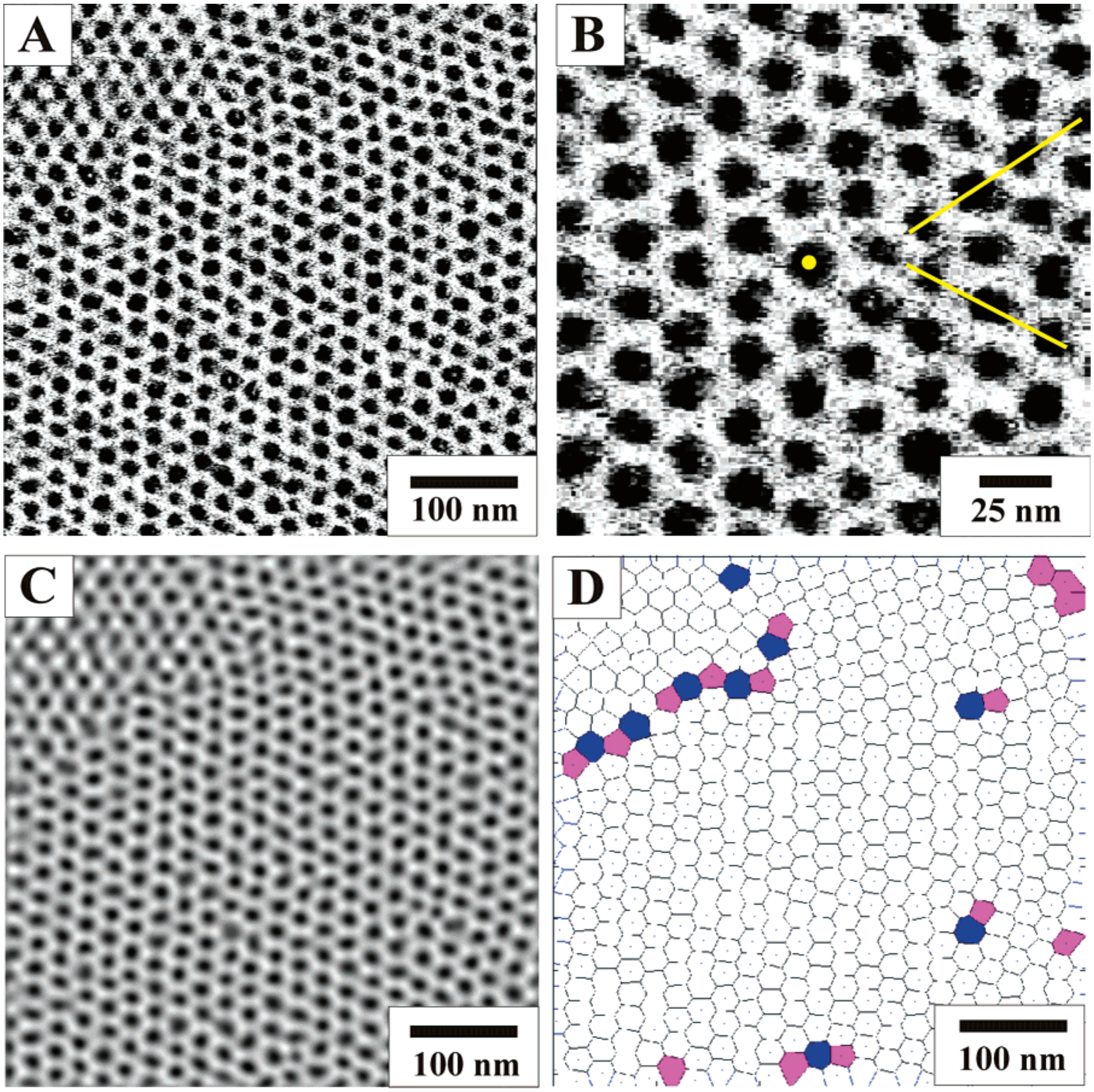

Figure 2. (A) Tapping Mode SFM phase image of an annealed CEC film. The vertical orientation of the cylinders within the film gives rise to the 2D hexagonal array of cylinder cores imaged here. (B) An enlarged view of an individual dislocation from the upper-right portion of (A). The yellow lines are drawn to indicate the additional half-rows of cylinders that terminate at the $-\pi/3$ disclination. The $+\pi/3$ disclination is indicated by the yellow dot. The cylinder cores of the $-\pi/3$ and $+\pi/3$ disclinations are markedly smaller and larger, respectively, than the cores of cylinders that are not at lattice defect sites. (C) The same image from (A) after Gaussian image enhancement. (D) The Voronoi diagram constructed from the array of cylinder core centroids obtained from (C). The $-\pi/3$ disclinations are denoted by five-sided polygons, colored magenta, and the $+\pi/3$ disclinations (seven-sided polygons) are colored blue. Note that at the image edges some cylinder cores are misidentified as having only five neighbors. This was corrected by hand before subsequent data handling.

tion from the cylinder core centroids (Figure 2D) obtained from Figure 2C allows for easy identification of the individual defect sites. Five-sided and seven-sided polygons, colored magenta and blue, respectively, represent the 5-fold and 7-fold coordinated cylinders that form the disclinations in the image. Thus, the PE domain area data obtained from the image could be separated into areas of the 5-, 6-, and 7-coordinated sites, normalized by the average 6-fold site area, $\langle A_6 \rangle$, and subjected to statistical analysis. The same treatment was applied to the Voronoi polygon area data. The majority of the data was obtained from disclinations found at grain boundaries. However, no statistically significant difference was found between data obtained at grain boundaries and that obtained from isolated dislocations.

The data from 21 such images (comprising observations from approximately 3000 6-fold sites and ca. 100 each of 5-fold and 7-fold sites) are represented in the normalized cylinder area distributions shown in Figure 3. Although each population is characterized by considerable polydispersity, the mean areas of the 5-, 6-, and 7-coordinated cylinder cores are significantly different (99.9% confidence level, as determined by Student's *t* test, population standard deviations not assumed to be equal). The analysis of the Voronoi cells (Figure 3B) yields narrower distributions of areas than the PE domain area analysis (Figure 3A). This result is unsurprising given that the Voronoi cell area analysis uses only the cylinder centroid positions as input and is therefore less significantly affected by problems related to image pixelation or the ambiguities of gray scale thresholding.

However, the two metrics also give significantly different values for the normalized areas at the 5- and 7-fold sites: the means of the 5- and 7-fold populations

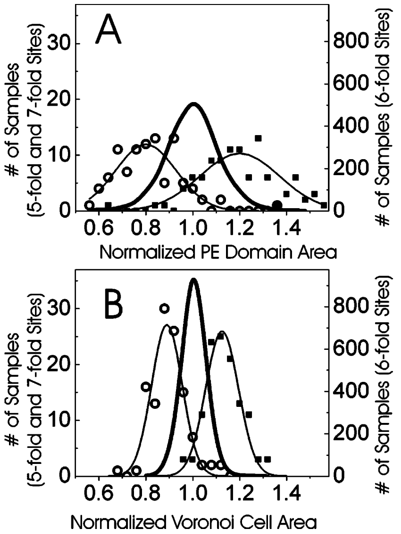

Figure 3. Distributions of the areas of the PE cylinder domains (A) and the areas of the Voronoi polygons (B). Distributions for 5-fold coordinated (open circles), 6-fold coordinated (dark solid line), and 7-fold coordinated (solid squares) cylinders are shown. Gaussian fits to the distribution data for 5-fold- and 7-fold coordinated cylinders are provided as guides to the eye. Statistics from these distributions are summarized in Table 1.

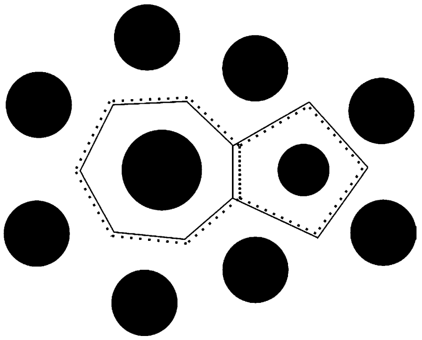

Figure 4. Schematic diagram showing the pitfalls of using the Voronoi cell area as a measure for the area of a cylinder core-plus-corona. The Voronoi cells are shown as solid lines and are drawn from the perpendicular bisectors of lines connecting domain centroids. The dotted lines represent points equidistant from the edges of adjacent domains, forming polygons that would yield better approximations for the cylinder sizes.

are closer to the 6-fold population mean for the Voronoi cell area analysis. Apparently, the use of the Voronoi cell as a proxy for the cross-sectional area of the cylinder core-plus-corona area is not entirely accurate. The Voronoi cell for a particular domain is constructed from the perpendicular bisectors of lines connecting the centroid of that domain to those of its nearest neighbors. However, to approximate the extent of the corona of a particular domain, we should use lines drawn equidistant from the domain *edges* rather than equidistant from the domain *centroids*. If all the PE domain cores are the same size, there is no difference between these two lines, but the situation changes when there is variability in the PE domain sizes. This effect is illustrated schematically in Figure 4. The Voronoi polygons drawn with lines equidistant to the domain centroids are shown as solid lines, while the dotted lines in the figure are drawn at points equidistant from the edges of adjacent domains. As the diagram indicates, the Voronoi polygons systematically underestimate the areas of 7-fold coordinated cylinders and overestimate those of 5-fold coordinated cylinders, in agreement with the experimental observations noted above.

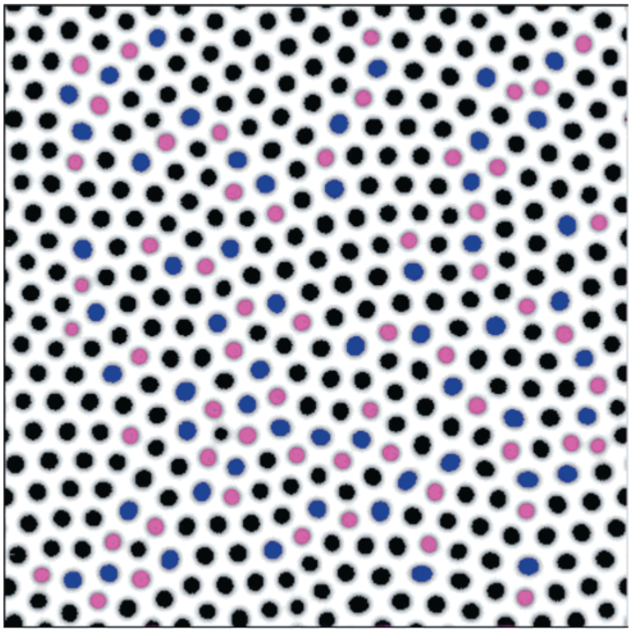

Figure 5. Results of the SCMFT simulation for a triblock copolymer closely resembling the CEC triblock used in the experimental portion of this work. Disclinations were identified by Voronoi analysis and are shown here in magenta ($-\pi/3$) and blue ($+\pi/3$).

The results of the SCMFT simulations are displayed in Figure 5. The 5-fold and 7-fold disclinations (as determined by Voronoi analysis) have been colored magenta and blue, respectively, for easy identification. Although the parameters used for the simulation were chosen to match the experimental conditions as closely as possible, the simulation result shows a significantly greater degree of lattice disorder than the experimental results. This is in part a consequence of a lack of coupling to a heat bath in the SCMFT algorithm, which prohibits the barrier crossing events necessary to anneal out defects. It is possible to provide such coupling to a thermal reservoir (“fluctuation effects”) by switching to a “complex Langevin” simulation in the chemical potential field variables,[25] in which case longer-ranged lattice order could in principle be achieved. However, we expect that the adjustment of domain sizes at disclination sites is primarily influenced by local forces, which the present simulation should reliably capture.

After subjecting the simulation results to the same domain area and Voronoi cell area analyses done with the experimental images, the area distributions shown in Figure 6 were obtained. Again, the analysis of the Voronoi cells yields narrower population distributions than the analysis of the areas of the B-block domains, and mean areas for the 5- and 7-fold sites which deviate less from the mean 6-fold site area, consistent with the arguments presented above for the experimental results. A summary of the experimental and simulation area data is contained in Table 1. The slight quantitative differences between simulation and experiment may be due to several factors, for example the inherent inaccuracies in SFM imaging or the absence of fluctuation effects in the SCMFT simulation. However, the qualitative agreement between simulation and experiment is excellent.

This size adjustment behavior at lattice defect sites has been observed previously in hexagonal arrays of

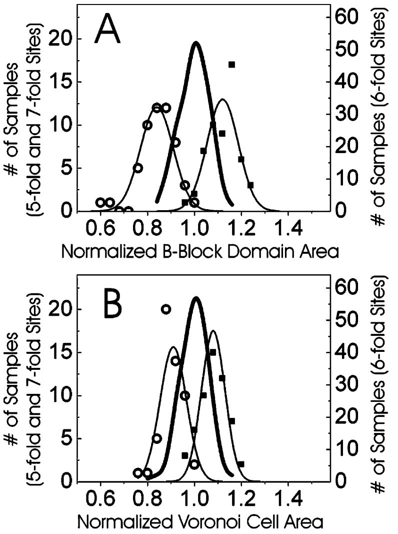

Figure 6. Distributions of cylinder areas obtained from the SCMFT simulation result: the areas of the minority phase domains (A) and the areas of the Voronoi polygons (B). Distributions for 5-fold coordinated (open circles), 6-fold coordinated (dark solid line), and 7-fold coordinated (solid squares) domains are shown. Gaussian fits to the distribution data for 5-fold and 7-fold coordinated cylinders are provided as guides to the eye. Statistics from these distributions are summarized in Table 1.

Table 1. Comparison of Domain Areas by Coordination Number

coord no., n	mean normalized area, $\langle A_n/\langle A_6\rangle\rangle$	sample std dev	95% confidence interval
	Experiment		
	PE domain area data		
5	0.80	0.13	0.03
6	1.00	0.11	0.005
7	1.20	0.17	0.03
	Voronoi polygon area data		
5	0.90	0.07	0.01
6	1.00	0.05	0.002
7	1.13	0.07	0.01
	Simulation		
	minority block domain area data		
5	0.84	0.07	0.02
6	1.00	0.06	0.01
7	1.12	0.07	0.02
	Voronoi polygon area data		
5	0.91	0.06	0.02
6	1.00	0.06	0.01
7	1.08	0.05	0.01

magnetic “bubble” domains formed in garnet films.[26,27] We note, however, that the symmetry of the copolymer domain area distributions about the average area of 6-fold sites, $\langle A_6\rangle$, stands in contrast to the asymmetric distribution observed for the magnetic “bubble” system, in which the 5-fold magnetic bubbles were distorted to a larger degree than were the 7-fold domains, i.e., $\langle A_6\rangle - \langle A_5\rangle > \langle A_7\rangle - \langle A_6\rangle$.

Summary

We have measured the nanodomain sizes of lattice defect sites in a 2D hexagonal array of vertically oriented triblock copolymer cylinders and compared the results with those of a 2D self-consistent mean-field theory simulation of a similar system. It is found that cylinder nanodomains at $-\pi/3$ (5-fold) and $+\pi/3$ (7-fold) disclinations contract and expand, respectively, in response to the local stress at the defect core. The degree of size adjustment appears to be independent of the context of the defect; that is, no difference is found between disclinations clustered at tilt grain boundaries and those paired in individual edge dislocations. Qualitative agreement between simulation and experiment is found.

Acknowledgment. This work was supported by the National Science Foundation DMR-Polymers Program under Grants DMR03-07233 and DMR03-12097 and a gift from the Dow Chemical Co. This work also made use of MRL Central Facilities supported by the NSF MRSEC Program under Award DMR00-80034. The authors thank C. Harrison (NIST) for suggesting the Voronoi polygon area analysis and A. Hexemer and R. Segalman for technical assistance regarding image analysis.

References and Notes

(1) Li, R. R.; Dapkus, P. D.; Thompson, M. E.; Jeong, W. G.; Harrison, C.; Chaikin, P. M.; Register, R. A.; Adamson, D. H. *Appl. Phys. Lett.* **2000**, *76*, 1689−1691.
(2) Cheng, J. Y.; Ross, C. A.; Chan, V. Z. H.; Thomas, E. L.; Lammertink, R. G. H.; Vancso, G. J. *Adv. Mater.* **2001**, *13*, 1174−1178.
(3) Kim, H. C.; Jia, X. Q.; Stafford, C. M.; Kim, D. H.; McCarthy, T. J.; Tuominen, M.; Hawker, C. J.; Russell, T. P. *Adv. Mater.* **2001**, *13*, 795−797.
(4) Morkved, T. L.; Lu, M.; Urbas, A. M.; Ehrichs, E. E.; Jaeger, H. M.; Mansky, P.; Russell, T. P. *Science* **1996**, *273*, 931−933.
(5) Thurn-Albrecht, T.; De Rouchey, J.; Russell, T. P.; Jaeger, H. M. *Macromolecules* **2000**, *33*, 3250−3253.
(6) Mansky, P.; Liu, Y.; Huang, E.; Russell, T. P.; Hawker, C. *Science* **1997**, *275*, 1458−1460.
(7) Huang, E.; Russell, T. P.; Harrison, C.; Chaikin, P. M.; Register, R. A.; Hawker, C. J.; Mays, J. *Macromolecules* **1998**, *31*, 7641−7650.
(8) Yang, X. M.; Peters, R. D.; Nealey, P. F.; Solak, H. H.; Cerrina, F. *Macromolecules* **2000**, *33*, 9575−9582.
(9) Heier, J.; Genzer, J.; Kramer, E. J.; Bates, F. S.; Walheim, S.; Krausch, G. *J. Chem. Phys.* **1999**, *111*, 11101−11110.
(10) Segalman, R. A.; Yokoyama, H.; Kramer, E. J. *Adv. Mater.* **2001**, *13*, 1152−1155.
(11) Carvalho, B. L.; Lescanec, R. L.; Thomas, E. L. *Macromol. Symp.* **1995**, *98*, 1131−1146.
(12) Kosterlitz, J. M.; Thouless, D. J. *J. Phys. C: Solid State Phys.* **1972**, L124−126.
(13) Kosterlitz, J. M.; Thouless, D. J. *J. Phys. C: Solid State Phys.* **1973**, *6*, 1181−1203.
(14) Halperin, B. I.; Nelson, D. R. *Phys. Rev. Lett.* **1978**, *41*, 121−124.
(15) Nelson, D. R.; Halperin, B. I. *Phys. Rev. B* **1979**, *19*, 2457−2484.
(16) Young, A. P. *Phys. Rev. B* **1979**, *19*, 1855−1866.
(17) Young, A. P.; Lavis, D. A. *J. Phys. A: Math. Gen.* **1979**, *12*, 229−243.
(18) Chaikin, P. M.; Lubensky, T. C. *Principles of Condensed Matter Physics*; Cambridge University Press: Cambridge, UK, 1995.
(19) Ohta, T.; Iwai, Y.; Ito, A.; Gunton, J. D. *Physica B* **1995**, *213*, 672−675.
(20) Hucul, D. A.; Hahn, S. F. *Adv. Mater.* **2000**, *12*, 1855−1858.
(21) Ruokolainen, J.; Fredrickson, G. H.; Kramer, E. J.; Ryu, C. Y.; Hahn, S. F.; Maganov, S. N. *Macromolecules* **2002**, *35*, 9391−9402.
(22) Segalman, R. A.; Hexemer, A.; Hayward, R. C.; Kramer, E. J. *Macromolecules* **2003**, *36*, 3272−3288.
(23) Drolet, F.; Fredrickson, G. H. *Phys. Rev. Lett.* **1999**, *83*, 4317−4320.
(24) Ryu, C. Y.; Ruokolainen, J.; Fredrickson, G. H.; Kramer, E. J.; Hahn, S. F. *Macromolecules* **2002**, *35*, 2157−2166.
(25) Fredrickson, G. H.; Ganesan, V.; Drolet, F. *Macromolecules* **2002**, *35*, 16−39.
(26) Seul, M.; Murray, C. A. *Science* **1993**, *262*, 558−560.
(27) Seul, M. *J. Phys. I* **1994**, *4*, 319−334.

MA026001O